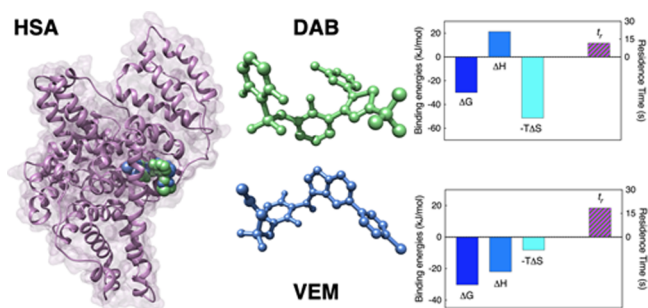


Binding of the B-Raf Inhibitors Dabrafenib and Vemurafenib to Human Serum Albumin: A Biophysical and Molecular Simulation Study

Maria Russi, Gabriele Cavalieri, Domenico Marson, Erik Laurini,* and Sabrina Pricl

ABSTRACT: Drug binding to human serum albumin (HSA) significantly affects *in vivo* drug transport and biological activity. To gain insight into the binding mechanism of the two B-Raf tyrosine kinase inhibitors dabrafenib and vemurafenib to HSA, in this work, we adopted a combined strategy based on fluorescence spectroscopy, isothermal titration calorimetry (ITC), circular dichroism (CD), and molecular simulations. Both anticancer drugs are found to bind spontaneously and with a 1:1 stoichiometry within the same binding pocket, located in Sudlow’s site II (subdomain IIIA) of the protein with comparable affinity and without substantially perturbing the protein secondary structure. However, the nature of each drug–protein interactions is distinct: whereas the formation of the dabrafenib/HSA complex is more entropically driven, the formation of the alternative vemurafenib/HSA assembly is prevalently enthalpic in nature. Kinetic analysis also indicates that the association rate is similar for the two drugs, whereas the residence time of vemurafenib within the HSA binding pocket is somewhat higher than that determined for the alternative B-Raf inhibitor.

KEYWORDS: B-Raf inhibitors, human serum albumin, fluorescence spectroscopy, isothermal titration calorimetry, circular dichroism, molecular simulations



1. INTRODUCTION

According to the American Cancer Society, by the end of 2021, about 106 200 new melanomas will be diagnosed in the United States (about 62 300 in men and 43 900 in women), with an expected death toll of approximately 7200 people (about 4600 men and 2600 women).¹ In Europe, approximately 26 100 men and 33 300 women are diagnosed with melanoma annually, with an estimated 8300 men and 7600 women losing their lives to the illness each year.² Cutaneous melanoma (CM) is the deadliest of all skin malignancies, with a median age at the time of diagnosis of 59 years. The prognosis of melanoma is largely determined by the stage at which the disease is discovered. When diagnosed early and treated appropriately, the prognosis of the localized disease (i.e., small thin lesions less than 1 mm in diameter without poor prognostic characteristics) is good, with more than 90% of patients surviving. At intermediate stages of the disease, 5 year disease-specific survival rates range from 63 to 81% in stage II CM (with most studies reporting a rate of over 70%), while the same parameter varies from 36 to 63% in stage III CM (with most studies reporting a rate of over 50%).³ Patients with unresectable or metastatic illness (stage IV CM), on the other hand, continue to have a dismal prognosis, with a 1 year

survival rate of 26% and a 5 year survival rate of less than 15%, with a median progression-free survival (PFS) of 1.7 months.⁴

The BRAF gene produces three Raf serine/threonine kinase (STK) isoforms (A-Raf, B-Raf, and C-Raf), all of which are involved in the mitogen-activated protein kinase (MAPK) signaling cascade regulating cell growth, differentiation, and survival.⁵ About 2 decades ago, melanomas were found to harbor several driver mutations in various members of the MAPK pathways, variations in BRAF being the most common event (approximately 50%). Among the most frequently observed BRAF mutations, the missense substitution V600E appears in 74–90% of cases, followed by V600K (15–25% of V600 mutations), V600R and V600D, although other rarer mutations (i.e., V600A, V600M, and V600G) have also been reported.⁶

Accepted: April 7, 2022

The therapeutic landscape for the treatment of metastatic melanoma has recently changed significantly with the approval for the clinical use of two drugs, dabrafenib (DAB) and vemurafenib (VEM), by the American Food and Drug Administration (FDA) and European Medicines Agency (EMA). Since 2013, both governmental agencies granted the use of the orally bioavailable dabrafenib (Tafinlar, GlaxoSmithKline) in patients with unresectable or metastatic melanoma harboring the specific B-Raf V600E mutation, although DAB is also active in wild-type B-Raf and the C-Raf isoform.⁷ Similarly, vemurafenib (Zelboraf, Roche)—another orally bioavailable chemical entity—was approved since 2011 for the clinical treatment of metastatic melanoma carrying the same V600E B-Raf mutation. Of note, VEM approval was extended in 2017 for its use as a treatment of adult patients affected by Erdheim–Chester disease (ECD), a quite rare histiocytosis recently recognized as a neoplastic disorder owing to the discovery of recurrent activating MAPK pathway alterations, B-Raf V600 mutations, in particular.⁸

Generally speaking, it is believed that the *in vivo* activity of a drug is regulated not just by its pharmacokinetics (PK) but also by pharmacodynamics (PD) properties, which may be affected by factors such as absorption, distribution, metabolism, and excretion (ADME). Several of these processes are strongly correlated with the property of the drug to bind plasma proteins (PPs), which, in turn, has an influence on the drug ADME features, eventually leading to different clinical results. Any drug binding to PPs presents benefits and pitfalls in terms of its efficacy and toxicity. For example, the free drug hypothesis generally assumes that the free (i.e., unbound) drug is in its biologically active form, while the protein-bound (inactive) component may operate as a reservoir and limit the amount of drug that can cross the plasma membranes to reach the target site. On the other hand, the drug/protein complexes can restrict possible drug side effects and use the unique circulation routes of the associated PPs to enhance the relevant PD properties. Under this perspective, the molecular and physiological processes underlying the binding of an anticancer drug to PPs should be investigated—both experimentally and theoretically—to the greatest possible extent to obtain fundamental information that can be translated into a deeper understanding of ADME behavior.⁹ For example, drug clearance and apparent volume of distribution are two PK characteristics that might undergo significant changes upon PP binding. In particular, most likely to be impacted in a clinical setting are those drugs endowed with high PP affinity and/or high intrinsic clearance (e.g., clearance by glomerular filtration). Accordingly, clinical regimens must be sensibly adjusted in response to these obstacles based on the specific PK/PD features of the drug administered.

In particular, it is generally accepted that plasma protein–drug interactions should be examined when the drug-bound fraction exceeds about 95% of the total drug concentration, as this might negatively affect the drug therapeutic index.¹⁰ Interestingly, when administered to humans, both DAB and VEM are highly bound to PPs (>99%), with comparable blood-to-plasma ratios (0.54 and 0.58, respectively); accordingly, the investigation of their PP binding behavior is of paramount importance in the context discussed a few lines above.

Human serum albumin (HSA) is the most prevalent protein in the blood plasma of all vertebrates, is produced in the liver as pre-pro-albumin, and develops in the endoplasmic reticulum

and Golgi bodies before being released by hepatocytes.^{11–13} With a normal plasma concentration of 30–50 g/mL and an approximate half-lifetime of 19 days,^{12,14,15} this protein is found in both extravascular and intravascular spaces where it performs a number of fundamental physiological functions including the regulation of blood pH and oncotic pressure and binding/transport of a wide range of endogenous and exogenous ligands of different nature (e.g., fats, hormones, amino acids, drugs, metabolites and nutrients, metal ions, and other proteins).^{11,14–16} Because of these characteristics, albumin is a promising option for a variety of clinical and biotechnological uses.

Especially for highly plasma-bound compounds such as the B-Raf inhibitors DAB and VEM, the anticancer drug interactions with HSA are critical in oncology targeted therapy since the amount of the unbound drug fraction is strictly connected to the actual concentration of the drug at its biological target site. Consequently, obtaining precise information on the HSA binding properties can play a pivotal role in a better understanding of their mode of action and their pharmacodynamics and pharmacokinetic characteristics.

Moreover, drug–HSA binding studies can be significant from a theoretical and practical standpoint because it allows for a better knowledge of the processes underlying medication bioavailability and elimination, as well as the impact of various pathological states or drugs on drug delivery and efficacy. Indeed, although no official clinical protocol considers yet the treatment of metastatic melanoma through the combination of DAB and VEM, other drugs may be coadministered in melanoma patients together with a B-Raf inhibitor. This combination can mutually alter the interaction profile with HSA and, if therapeutic windows are particularly narrow, this can lead to dramatic effects for the patient.

Accordingly, in this work, we present for the first time the results obtained from a combined experimental/computational approach aimed at investigating the binding properties of the two clinically approved B-Raf inhibitors DAB and VEM to HSA. From the experimental standpoint, we performed steady-state fluorescence quenching experiments and isothermal titration calorimetry (ITC) to characterize the binding thermodynamics and kinetics of both anticancer drugs to HSA. Far-ultraviolet circular dichroism (far-UV CD) spectroscopy was adopted to determine eventual conformation changes induced in the protein structure by drug binding, whereas competitive site marker displacement experiments along with molecular simulations led us to define the binding site and mode of these two B-Raf inhibitors with this fundamental human protein.

2. MATERIALS AND METHODS

2.1. Reagents and Chemicals. Globulin and fatty acid-free HSA (A1887) were obtained from Sigma-Aldrich Inc. (Saint Louis, MO), while DAB, VEM, indomethacin (IND), ketoprofen (KET), and hemin (HEM) were obtained from MedChemExpress (Monmouth, NJ). All other reagents and chemicals (analytical grade) were also purchased from Sigma-Aldrich.

2.2. Sample Preparation and Analytical Procedures. A stock solution of HSA was prepared by dissolving a specific amount of protein in phosphate buffer saline 1× (PBS, pH = 7.4), and the protein concentration was determined via UV spectroscopy using a value of 35 700 M⁻¹ cm⁻¹ for the molar extinction coefficient at wavelength $\lambda = 280$ nm.^{17,18} Similarly,

stock solutions of DAB, VEM, IND, KET, and HEM were prepared in ethanol. All stock solutions were maintained in the dark and at 4 °C.

2.3. Ultraviolet–Visible (UV–Vis) Spectroscopy. The ultraviolet–visible (UV–vis) absorption spectra of HSA, dabrafenib, and vemurafenib were recorded on a DS11-FX spectrophotometer (DeNovix Inc., Wilmington, DE) at room temperature (298 K).

2.4. Steady-State Fluorescence Spectroscopy. All fluorescence measurements were carried out using a J-1500 spectropolarimeter (Jasco, Japan) equipped with a thermostated cell holder, an FDT-538 fluorescence emission detector, and a 0.1 cm quartz cell. The excitation wavelength (λ_{exc}) was set to 280 nm, and the fluorescence spectra were recorded in the range of 300–450 nm at three temperatures (298, 304, and 310 K) using 5/10 nm slit widths. During all fluorescence quenching titrations, the concentration of HSA was kept fixed at 2 μM , while the concentrations of DAB and VEM were varied from 0 to 6 μM at increments of 1 μM . Each drug/protein solution was allowed to incubate for 1 h before recording the corresponding fluorescence spectrum. All fluorescence data were corrected for the inner filter effect according to the following equation¹⁹

$$F_{\text{corr}} = F_{\text{obs}} \times 10^{(A_{\text{exc}} + A_{\text{em}})/2} \quad (1)$$

in which F_{corr} and F_{obs} are the corrected and observed fluorescence intensities, respectively, while A_{exc} and A_{em} are the absorption of the systems at the excitation (280 nm) and the emission (343 nm) wavelengths, respectively. Control experiments were carried out to check the influence of ethanol and pristine drugs. As shown in Figure S1, the solvent, at its higher tested concentration, did not affect substantially the fluorescence spectra of HSA, while both DAB and VEM have no significant emission in the range of 300–450 nm at the same experimental conditions.

2.5. Far-UV Circular Dichroism Spectroscopy. Far-UV circular dichroism (CD) spectra were recorded from 200 to 260 nm at a scan rate of 20 nm min^{-1} and at three temperatures (298, 304, and 310 K) on a J-1500 spectropolarimeter (Jasco, Japan) equipped with a thermostated cell holder and a PML-534 FDCD detector. The path length cell was 0.1 cm, while the step size and bandwidth were set to 0.5 and 1 nm, respectively. The observed spectra were corrected for baseline (pure buffer solution), and the final CD curves are presented as the average of three repetitions. All spectra were visualized and analyzed with Jasco Spectra Manager software. The fractional content of the secondary structure elements of the HAS, in the presence and absence of the two drugs, was calculated in the CD Multivariate SEE program using the standard calibration models.

2.6. Competitive Site Marker Displacement Experiments. Competitive site marker displacement studies were carried out with the three different HSA binding site markers IND, KET, and HEM—specific site markers for binding sites I, II, and III, respectively.^{20,21} In these experiments, DAB or VEM (0–6 μM) was gradually added to a cosolution of HSA (2 μM) and a marker (2 μM), respectively, and the relevant fluorescence quenching data were collected following the same methodology described in Section 2.4.

2.7. Isothermal Titration Calorimetry Studies. Isothermal titration calorimetry (ITC) experiments were performed with a MicroCal PEAQ-ITC calorimeter (Malvern,

U.K.) at 298 K (cell volume = 208 μL). Thermodynamics of the HSA/drug complex formation was investigated in PBS buffered solutions. Specifically, a solution of HSA (20 μM , sample cell) was titrated with 19 step-by-step injections of 2 mL volume of each inhibitor (200 μM , syringe). Solutions and buffer were degassed for 30 min at room temperature under stirring at 700 rpm prior to each experiment. Unspecific heats were further measured by control experiments (data not shown) and, accordingly, they were subtracted from the relevant data set to yield the corrected integrated data. All experiments were run in triplicate. For kinITC analysis, the AFFINmeter software suite (v2.1802.S, Software for Science Developments, Spain) was used.^{22–25} Data acquisition and analysis were performed using GraphPad Prism 8.0.0 for Mac (GraphPad Software, San Diego, CA, www.graphpad.com).

2.8. Molecular Simulations. 2.8.1. Preparation of the Molecular Models. The crystal structure of HSA was downloaded from the RCSB Protein Data Bank,²⁶ with PDB ID 4K2C.²⁷ The H⁺ webserver²⁸ (<http://biophysics.cs.vt.edu/H++>) was used to obtain the physiological protonation state of the relevant protein residues. The molecular models of DAB and VEM were built and optimized using Avogadro software;²⁹ then, they were parameterized with the gaff2 forcefield³⁰ using the antechamber program from AMBER20³¹ for the correct atom-type assignment. The RED server³² was employed to derive atomic partial charges following the RESP procedure.³³ The tleap software within the AMBER20 platform²⁹ was used to parameterize the protein (*via* the ff14SB forcefield³⁴), as well as its complexes with DAB and VMF. Within tleap, each system was also solvated in boxes of TIP3PB water molecules³⁵ with dimensions spanning at least 1.4 nm from each atom of each solute. An appropriate number of sodium and chlorine ions were added to reach a physiological salt concentration of 0.15 M. To relax the crystal structure of HSA prior to drug docking with each compound (production run lasting 100 ns) and to equilibrate each protein/drug complex prior to metadynamics simulations (production runs lasting 500 ns), the following simulation scheme was adopted. The simulation box was first energy-minimized, each minimization stage consisting of 3000 steps of steepest descent followed by 3000 steps of conjugated gradient algorithms while applying a weak restraint (41.8 kJ/mol) on the proteins' backbone atoms (and on the drug atoms as well during drug/complex optimization). A second run of minimization was performed, removing all of the restraint on the solute. Molecular dynamics (MD) runs were then performed while re-establishing the restraints to the protein backbone atoms (and the drugs when present) in the canonical (NVT) ensemble for 10 ps, heating the system to 150 K. A further heating stage to a production temperature of 300 K followed (50 ps), switching to the isothermal/isobaric ensemble (NPT, $P = 1 \text{ atm}$ maintained by the Berendsen barostat³⁶). Five further steps of short MD simulations (100 ps) were carried out while gradually removing the restraints (–8.37 kJ/mol per step). Once all of the restraints were removed, 10 ns of MD simulations was carried out under NPT conditions, followed by MD production runs during which pressure was maintained using the Monte Carlo barostat implemented in AMBER. During all of the MD stages, electrostatic interactions were computed by means of the particle mesh Ewald (PME) algorithm,³⁷ while the temperature was regulated by the Langevin method³⁸ (collision frequency of 2.5 ps^{-1}). The SHAKE algorithm³⁹ was applied to

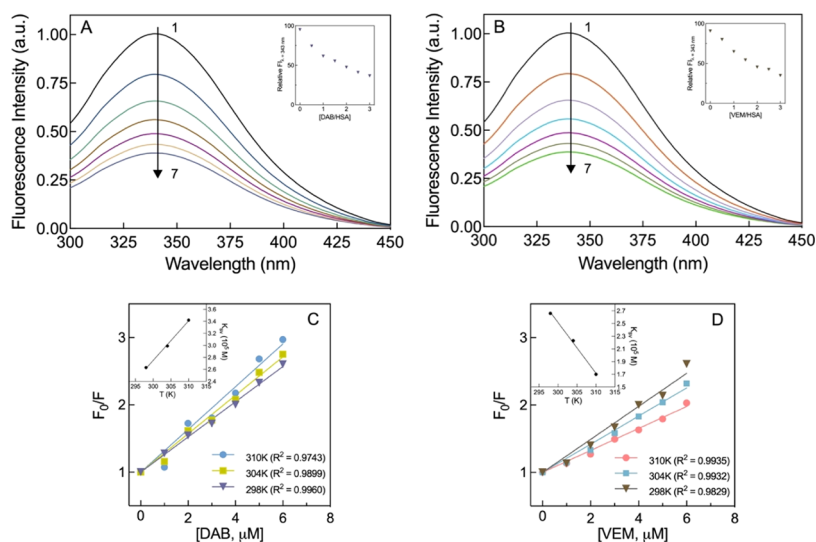


Figure 1. (Top panel) Steady-state fluorescence quenching of HSA ($2 \mu\text{M}$) in the presence of increasing concentrations ($0\text{--}6 \mu\text{M}$) of the two B-Raf inhibitors DAB (A) and VEM (B) (PBS buffer, $\text{pH} = 7.4$, $T = 298 \text{ K}$, and $\lambda_{\text{exc}} = 280 \text{ nm}$). The insets show the decrease in HSA relative fluorescence intensity at the peak wavelength ($\lambda = 343 \text{ nm}$) as a function of increasing inhibitor/protein molar ratios. (Bottom panel) Stern–Volmer plots for HSA fluorescence quenching induced by DAB (C) and VEM (D) at three different temperatures (298, 304, and 310 K). The inset represents the plot of K_{SV} vs T .

allow for a 2 fs integration time step during the final equilibration and production runs (during the heating stage, a 1 fs time step was employed). The pmemd module of AMBER20 running on the supercomputer Marconi100 (CINECA, Bologna, Italy) and on our central processing unit/graphics processing unit (CPU/GPU) hybrid cluster was used for all of the minimization and MD stages.

2.8.2. Drug Docking. The MD-equilibrated structure of HSA was used to perform DAB and VEM docking with the Autodock Vina program.⁴⁰ The search space for the docking computations was restricted to the subdomain IIIA (binding site II), in agreement with the results obtained from the site marker competition studies. The exhaustiveness parameter was increased to 25, and the number of solutions was increased to 15, while the other parameters were left to their default values. For both drugs, the resulting ligand/protein complex conformation characterized by the lowest-scoring energy was carried on to the subsequent MD and metadynamics experiments. The UCSF Chimera software⁴¹ was used to visualize the docking results, as well as to produce all of the molecular images.

2.8.3. Metadynamics Simulations. The frequency adaptive metadynamics (FaMetaD) approach⁴²—an evolution of the computational method originally proposed by Parrinello and co-workers⁴³ based on infrequent metadynamics (InMetaD)—was adopted to determine the residence times of both DAB and VEM within the HSA binding site. The simulations were carried out using the open-source, community-developed PLUMED library⁴⁴ (version 2.7.1⁴⁵), according to the well-tempered metadynamics approach (bias factor = 15). Two reaction coordinates (RCs) were considered to drive the drug unbinding process, the first (RC1) being the distance between the center of mass (CoM) of the drug and the CoM of the Ca atoms of the residues shaping the protein binding pocket (defined as the residues with heavy atoms within 5 Å of the drug). As a second RC (RC2), we selected the number of water molecules surrounding the drug as a representation of the hydration status of the molecule during unbinding.

Accordingly, RC2 was defined as the number of water molecules within 8.0 Å from the drug CoM, computed with the default PLUMED switching function with 3.0 and 8.0 Å for the d_0 (i.e., the distance at which the switching function begins to decay) and r_0 (the distance at which the switching function attains the zero value) parameters, respectively. The Gaussian width was set to 0.05 Å and 0.1 for RC1 and RC2, respectively. A value of 4.2 kJ/mol was chosen for the initial hill height, and the initial Gaussian deposition time was 1 ps. The threshold value of the acceleration factor at which the FaMetaD was started was set to 10^5 . All values reported are obtained from a bootstrap analysis with 100 subsamples. To assess the reliability of the computed times, the distribution of results obtained from different independent simulations (15) was checked according to a Poisson distribution⁴⁶ using a Kolmogorov–Smirnov (KS) test. Each simulation was started with the drug bound to HSA, and it stopped when complete drug unbinding was observed.

3. RESULTS AND DISCUSSION

3.1. Fluorescence Quenching of HSA Induced by DAB and VEM.

The fluorescence quenching of aromatic amino acids is an efficient tool for determining the binding affinity and mechanism underlying ligand–protein interactions.^{47–51} Indeed, when compared to alternative biophysical and biochemical methods for evaluating protein/ligand interaction, fluorescence quenching provides several advantages.^{52,53} For instance, fluorescence intensity is directly proportional to the number of fluorophores present in a sample, which enables quantitative measurements. Also, fluorescence measurements have a very high sensitivity and may therefore be carried out on single molecules, allowing for the observation of biological mechanisms at the molecular level.⁵⁴ Moreover, fluorescence is a phenomenon that is governed by a number of different factors that may be measured individually or in combination to gather information not only on the presence of a given fluorophore but also on its orientation and its proximate environment. When excited at a wavelength of $\lambda = 280 \text{ nm}$,

Table 1. Stern–Volmer Constants (K_{SV}) and Bimolecular Quenching Rate Constants (k_q) for HSA Tryptophan Fluorescence Quenching by DAB and VEM at Different Temperatures

DAB			VEM		
T (K)	K_{SV} ($10^5 M^{-1}$)	k_q ($10^{13} M^{-1} s^{-1}$) ^a	T (K)	K_{SV} ($10^5 M^{-1}$)	k_q ($10^{13} M^{-1} s^{-1}$) ^a
298	2.63 ± 0.03	4.70	298	2.66 ± 0.08	4.74
304	2.99 ± 0.04	5.34	304	2.23 ± 0.05	3.99
310	3.42 ± 0.07	6.11	310	1.70 ± 0.03	3.04

^aAs mentioned in the text, here the value of $\tau_0 = 5.6$ ns for HSA was adopted for the calculation of k_q in agreement with our previous work.⁶³ We note that an alternative value for this parameter (6.38 ns) has also been reported⁶⁸ and employed in some studies (e.g., ref 56); however, the use of either value of τ_0 has no effect on the relevant discussion as the order of magnitude of the corresponding k_q is unaffected.

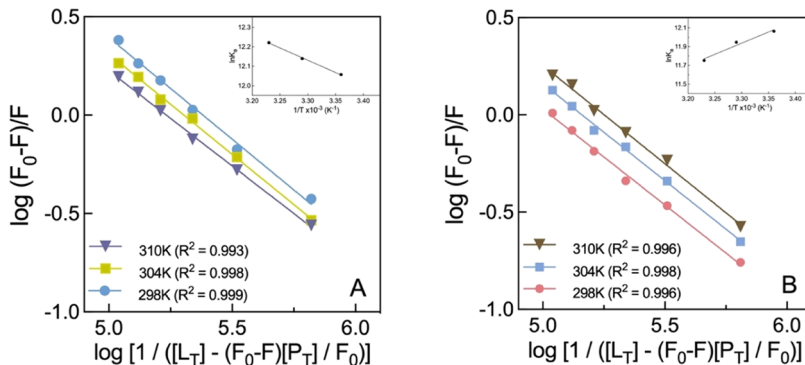


Figure 2. Plots of $\log(F_0 - F)$ vs $\log [1/([L_T] - (F_0 - F)[P_T]/F_0)]$ for HSA fluorescence quenching by DAB (A) and VEM (B) at three different temperatures (298, 304, and 310 K). The insets show the corresponding van't Hoff plots ($\ln K_a$ vs $1/T$; see eq 6) for DAB/HSA and VEM/HSA interactions, respectively.

HSA exhibits a distinctive emission maximum at $\lambda = 343$ nm, and the unique HSA tryptophan residue at position 214 (W214), located at Sudlow's site I in subdomain IIA, is responsible for this intrinsic protein fluorescence feature.⁵⁵ Figure 1 shows the fluorescence spectra of HSA ($2 \mu M$) recorded at $25^\circ C$ alone and in the presence of increasing concentrations (0 – $6 \mu M$) of DAB (panel A) and VEM (panel B). As it can be seen from this figure, the progressive addition of each B-Raf inhibitor to the protein results in a gradual, concentration-dependent reduction of the W214 fluorescence intensity with no detectable shift in the HSA emission maximum wavelength or peak shape along the entire titration process. At the highest drug concentration employed ($6 \mu M$), approximately 65% of W214 fluorescence quenching is observed in both cases (see the insets in Figure 1A,B), supporting the formation of steady-state DAB/HSA and VEM/HSA complexes. Of note, free DAB and VEM solutions do not exhibit fluorescence emission in the 300 – 450 nm range of wavelength, and other HSA fluorescence quenching data were previously described in the literature after interactions with several tyrosine kinase inhibitors or other drugs reporting no visible shifts/changes in the protein emission maximum.^{56–61}

In situations where the fluorophore and quencher are distinct molecular entities (i.e., not connected by covalent bonds) and typically exist in either an unquenched state (where they are free to diffuse randomly and independently) or a quenched state (where they form a noncovalent molecular complex), two quenching limits may be defined: collisional quenching (CQ, commonly referred to as dynamic quenching) and binding-related quenching (BRQ, also known as static quenching).⁶² While diffusion is required in the CQ mechanism to bring the quencher close enough to the fluorophore to cause detectable quenching, during a BRQ process, the existence of noncovalent binding interactions

between the quencher and fluorophore is robust enough that a significant population is within the quenching distance at the time of excitation, allowing the quenching process to begin immediately after excitation. Another widely accepted general assumption is that the temperature dependency of BRQ and CQ may be used to differentiate the two mechanisms. This relies on the simplifying hypothesis that the diffusion coefficient, which regulates CQ, and the binding equilibrium constant, which controls BRQ, are the sole temperature-dependent parameters. However, under the condition that the temperature dependence of the fluorescence yield can be neglected, CQ would increase as the temperature T increases while BRQ would decrease, with the remarkable exception of entropy-driven binding for which BRQ would reveal an opposite trend.⁶²

Accordingly, to further investigate the quenching mechanism involved in the interaction between HSA with the two B-Raf inhibitors, protein fluorescence quenching data obtained at three different temperatures (i.e., 298, 304, and 310 K) were analyzed *via* the well-known Stern–Volmer equation

$$F_0/F = 1 + k_q\tau_0[Q] = 1 + K_{SV}[Q] \quad (2)$$

in which F_0 and F are the fluorescence peak intensities of the fluorophore (W214 of HSA) in the absence and presence of a quencher, respectively, k_q is the bimolecular quenching rate constant, τ_0 is the average lifetime of the protein (5.6 ns for HSA^{63–67}), and $[Q]$ is the concentration of the quencher (here DAB and VEM, respectively). The product of k_q and τ_0 in eq 2 is also known as the Stern–Volmer quenching constant K_{SV} . The Stern–Volmer plots for the HSA fluorescence quenching by DAB and VEM are reported in Figure 1C,D, while the corresponding calculated values of K_{SV} and k_q are listed in Table 1.

Table 2. Binding Parameters of HSA with DAB and VEM Derived from Fluorescence Quenching Data Using eq 3 and from the van't Hoff Plots (Insets in Figure 2)^a

DAB/HSA						
T (K)	K_a ($10^5 M^{-1}$)	n	ΔG_b (kJ/mol)	ΔH_b (kJ/mol)	ΔS_b (J/(mol K))	ΔG_b (kJ/mol)
298	1.72 ± 0.03	0.968 ± 0.06	-29.87	+10.50	+135.4	-29.84
304	1.85 ± 0.03	1.02 ± 0.09	-30.67			-30.65
310	2.03 ± 0.06	1.03 ± 0.07	-31.46			-31.46
VEM/HSA						
T (K)	K_a ($10^5 M^{-1}$)	n	ΔG_b (kJ/mol)	ΔH_b (kJ/mol)	ΔS_b (J/(mol K))	ΔG_b (kJ/mol)
298	1.74 ± 0.03	1.01 ± 0.11	-29.87	-19.85	+34.0	-29.91
304	1.54 ± 0.02	0.996 ± 0.08	-30.17			-30.11
310	1.27 ± 0.04	0.988 ± 0.07	-30.29			-30.31

^aThe values of ΔG_b in the fourth column are directly calculated from the relevant K_a values *via* eq 4. The values of ΔG_b in the last column are derived from the ΔH_b and ΔS_b values obtained from the corresponding van't Hoff plots (eq 6) using eq 5.

As can be seen from Table 1, the values of k_q estimated using eq 2 for both B-Raf inhibitors at the three temperatures are all on the order of $10^{13} M^{-1} s^{-1}$ and hence substantially higher than the maximum CQ rate constant ($2.06 \times 10^{10} M^{-1} s^{-1}$) reported for the association of different quencher/fluorophore systems,^{19,69} suggesting a BRQ as the underlying mechanism for both DAB/HSA and VEM/HSA interactions. Interestingly, however, while for the DAB/HSA complex, an inverse correlation of k_q (and hence K_{SV}) with temperature is observed, the reverse trend is noted for the alternative VEM/HSA complex, with k_q (and K_{SV}) values increasing with increasing T (Figure 1 and Table 1). According to what was discussed a few lines above, this suggests that while BRQ is still in place, entropy might play a substantial role in promoting the formation of the VEM/HSA assembly (*vide infra*).

3.2. Determination of Binding Constants and Thermodynamics for DAB/HSA and VEM/HSA Based on Fluorescence Quenching Data. For BRQ and under the assumption that there are n equivalent and independent binding sites for a given quencher Q on a given protein, the binding constant K_a for each of the two B-Raf inhibitors onto HSA can be calculated from the relevant fluorescence quenching data according to the following double logarithmic equation⁷⁰

$$\log(F_0 - F)/F = n \log K_a - n \log[1/([L_T] - (F_0 - F)[P_T]/F_0)] \quad (3)$$

where F_0 and F again denote the protein steady-state fluorescence in the absence and presence of a quencher, respectively, n is the number of quenchers (*i.e.*, ligands) bound to the protein, K_a is the binding constant, while $[L_T]$ and $[P_T]$ are the total ligand and total protein concentration, respectively. Figure 2 shows the resulting double logarithmic plots obtained for DAB/HSA and VEM/HSA at the three temperature values considered, while the corresponding values of K_a and n are listed in Table 2. As seen from this table, in the temperature range analyzed, the affinities of DAB and VEM for HSA are comparable, with K_a values on the order of $10^5 M^{-1}$, suggesting a moderate protein/drug affinity that could be beneficial for drug transport and release by this protein; also, the number of binding sites n is always very close to one, indicating that there is only one preferential ligand binding site on the protein surface (1:1 stoichiometry) for both complexes. Finally, in parallel with the temperature-dependent behavior observed for K_{SV} , an opposite trend is seen for the values of

$K_a(T)$ in the two cases, with a common inverse K_a - T correlation for VEM/HSA interactions and a (less frequently observed) direct correlation of K_a with T for the alternative DAB/HSA system, further supporting the evidence of an entropy-driven binding process underlying the latter drug/protein association.

To investigate in detail the nature of the binding interactions associated with the formation of the DAB/HSA and VEM/HSA complexes, data in Table 2 were further elaborated to derive the main thermodynamic parameters—*i.e.*, the variation of binding enthalpy (ΔH_b), entropy (ΔS_b), and free energy (ΔG_b)—using the van't Hoff plots. Indeed, while the sign of ΔG_b is a hallmark of the thermodynamic spontaneity of a chemical process at a given T (with $\Delta G_b < 0$ for thermodynamically spontaneous events), based on the distinctive signs of ΔH_b and ΔS_b , it is also possible to broadly classify the dominating contact forces between small ligands and proteins into three main categories: hydrophobic interactions (for which $\Delta H_b > 0$, $\Delta S_b > 0$), H-bond/polar interactions ($\Delta H_b < 0$, $\Delta S_b > 0$), and van der Waals interactions ($\Delta H_b < 0$, $\Delta S_b < 0$).⁷¹ In the limited range of temperature values such as those considered in the present work ($\Delta T = 12$ K), and for reversible binding reactions, both ΔH_b and ΔS_b can be reasonably assumed to be independent of T , so that by combining the Gibbs free-energy isotherm

$$\Delta G_b = -RT \ln K_a \quad (4)$$

with the well-known expression for the Gibbs free energy of reaction

$$\Delta G_b = \Delta H_b - T\Delta S_b \quad (5)$$

a linear relationship between $\ln K_a$ and $1/T$ is obtained as

$$\ln K_a = -\Delta H_b/RT + \Delta S_b/R \quad (6)$$

where R is the universal gas constant ($8.31 J/(mol K)$). Accordingly, by plotting $\ln K_a$ vs $1/T$, the values of ΔH_b and ΔS_b can be directly obtained from the slope and the intercept of the relevant linear fits (van't Hoff plots; see the insets in Figure 2), while the corresponding free energies of binding can be readily obtained through eq 5. The last three columns of Table 2 summarize these results. As it can be seen, the formation of both drug/protein complexes is thermodynamically spontaneous (*i.e.*, $\Delta G_b < 0$) at all temperatures. Importantly, however, this analysis also reveals that in the case of the VEM/HSA complex, both the negative ΔH_b (-19.85 kJ/mol) and positive ΔS_b ($+34.0$ J/(mol K)) values

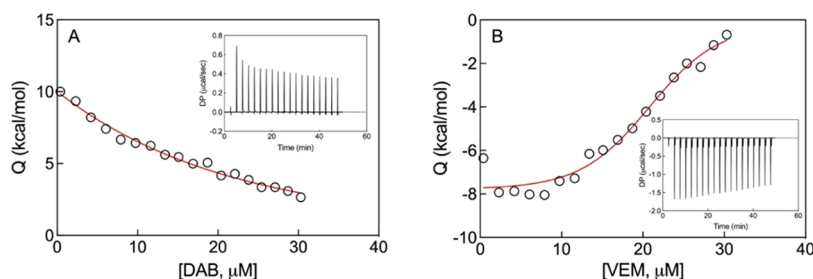


Figure 3. Plots of the integrated area under each ITC peak for the interaction between DAB (A) and VEM (B) with HSA at 298 K ([HSA] = 20 μ M, PBS buffer, pH = 7.4). The solid line is the model data fitting with the one-site (1:1 binding stoichiometry) isothermal binding model (insets: ITC raw data).

Table 3. Thermodynamic (ΔH_{b-ITC} , ΔS_{b-ITC} , ΔG_{b-ITC} , n , K_{a-ITC}) and Kinetic (k_{on} , k_{off} , t_r) Parameters for the Binding of DAB and VEM to HSA as Obtained from ITC Experiments at 298 K^a

DAB/HSA									
ΔH_{b-ITC} (kJ/mol)	ΔS_{b-ITC} (J/(mol K))	ΔG_{b-ITC} (kJ/mol)	n	K_{a-ITC} ($10^5 M^{-1}$)	k_{on} ($10^4 M^{-1} s^{-1}$)	k_{off} ($10^{-2} s^{-1}$)	t_r (s)	$t_{r,sim}$ (s)	
$+21.42 \pm 0.24$	$+172.8$	-30.08	1.2 ± 0.14	1.86	1.57	8.44	11.8	5.73 ± 2.5	
VEM/HSA									
ΔH_{b-ITC} (kJ/mol)	ΔS_{b-ITC} (J/(mol K))	ΔG_{b-ITC} (kJ/mol)	n	K_{a-ITC} ($10^5 M^{-1}$)	k_{on} ($10^4 M^{-1} s^{-1}$)	k_{off} ($10^{-2} s^{-1}$)	t_r (s)	$t_{r,sim}$ (s)	
-22.05 ± 0.31	$+27.78$	-30.33	1.1 ± 0.10	2.06	1.12	5.42	18.5	14.0 ± 6	

^aThe last column in this table shows the drug residence time $t_{r,sim}$ estimated by molecular simulations (see Section 3.5.3). All ITC experiments were run in triplicate. Errors on ΔH_b are within 10%.

favor drug/protein binding, with an apparent balanced contribution between H-bond/polar and hydrophobic forces in modulating the affinity of VEM for HSA in the framework of this approach (see Sections 3.3 and 3.5.3). On the contrary, for the alternative DAB/HSA system, the analysis reports both positive values of ΔH_b (+10.50 kJ/mol) and ΔS_b (+135.4 J/(mol K)), with a prevailing favorable entropic contribution to ΔG_b . This clearly indicates that, in agreement with the other evidence discussed above, binding this B-Raf inhibitor to HSA is an entropy-driven process mainly governed by hydrophobic interactions (see also Sections 3.3 and 3.5.3). Of note, the validity of the assumption of a negligible temperature dependency of ΔH_b and ΔS_b in the ΔT range studied here was verified by calculating the values of ΔG_b for both drug/protein complexes at all temperatures using eq 4 (fourth column in Table 2) and successfully comparing these data with the ΔG_b values derived by eq 5 (last column in Table 2).

3.3. Thermodynamics and Kinetics of Binding of HSA with DAB and VEM via Isothermal Titration Calorimetry (ITC). ITC is a very sensitive biophysical method that measures the heat released or absorbed in a reactive system as a function of the quantity of the added reactant. During the last decade, ITC has been widely acknowledged as a gold-standard technique for examining intermolecular and/or intramolecular interactions.^{72–78} For each association/dissociation process, it concurrently provides the three main thermodynamic parameters (ΔH_{b-ITC} , ΔS_{b-ITC} , and ΔG_{b-ITC}), the binding affinity K_{b-ITC} , and the reaction stoichiometry (or number of binding sites) n . It has to be observed at this point that these affinity measurements are determined under close system (*in vitro*) conditions, where the drug and its protein target are at equilibrium;⁷⁹ as such, they cannot fully account for drug/protein interactions *in vivo*, where the concentrations of both the ligand and its target can change during normal function and/or in the presence of the active principle.⁸⁰ Therefore, if a given drug and its protein target are not at equilibrium, *in vitro* binding measurements based only on thermodynamic

parameters *per se* are unlikely to fully describe the real situation in the nonequilibrium (open) environment represented by the human body. On the other hand, experimental strategies assessing both the thermodynamics and kinetics aspects of drug/protein interactions are more likely to reflect an *in vivo* situation; in particular, the determination/estimation of the lifetime of the relevant drug/protein complex is of paramount importance since a drug will only exert its effect when bound to its target.^{81,82} In this perspective, the so-called residence time t_r —the reciprocal of the rate constant for drug/target complex dissociation k_{off} —is the most convenient nonequilibrium intrinsic parameter to quantify the lifetime of a given drug/protein ensemble.^{79,83–87}

Accordingly, ITC experiments were initially performed to determine the binding thermodynamics of DAB and VEM to HSA at room temperature, and the results are shown in Figure 3 and Table 3.

As seen from Figure 3, for both systems considered, the integrated raw heat data can be well fitted to the one-site (1:1 binding stoichiometry) isothermal binding model, and the ITC-derived values of the binding constant K_{a-ITC} , free energy of binding ΔG_{b-ITC} , and stoichiometry n at 298 K ($K_{a-ITC} = 1.86 \times 10^5 M^{-1}$, $\Delta G_{b-ITC} = -30.08$ kJ/mol, $n = 1.2$ and $2.06 \times 10^5 M^{-1}$, $\Delta G_{b-ITC} = -30.33$ kJ/mol, $n = 1.1$ for DAB/HSA and VEM/HSA, respectively; Table 3) are in excellent agreement with those estimated from the corresponding fluorescence quenching data at the same temperature using eq 3 (see Table 2). Accordingly, ITC data support the spontaneous formation of both drug/protein assemblies with a 1:1 stoichiometry. When compared to those generated through temperature-dependent fluorescence quenching study, the values of the other two ITC-derived binding thermodynamic parameters— $\Delta H_{b-ITC} = +21.42$ kJ/mol and $\Delta S_{b-ITC} = +172.8$ J/(mol K) for DAB/HSA and $\Delta H_{b-ITC} = -22.05$ kJ/mol and $\Delta S_{b-ITC} = +27.78$ J/(mol K) for VEM/HSA, respectively—are also within the same order of magnitude (see Table 2). Most importantly, however, ITC experiments confirm the different

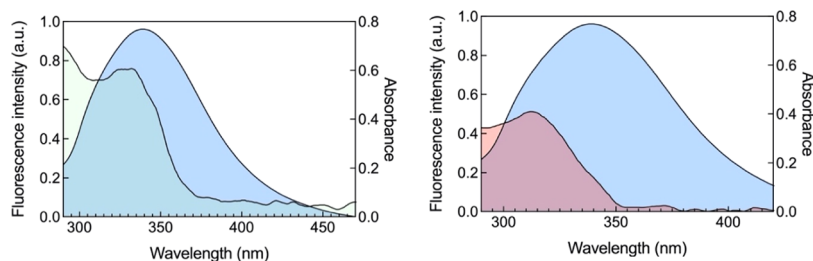


Figure 4. Overlap between the fluorescence emission spectrum of HSA (light blue curve, left axis) and (left) the absorption spectrum of DAB (light green curve) and (right) the absorption spectrum of VEM (light red curve) at 298 K.

contributions of the interaction forces driving the association between the two B-Raf inhibitors with HSA discussed above on the basis of steady-state fluorescence quenching data. Indeed, for VEM/HSA binding, ΔH_{b-ITC} is <0 and larger than the corresponding $T\Delta S_{b-ITC}$ term (*i.e.*, $+8.28$ kJ/mol = $(298$ K \times 27.78 J/(mol K)/1000); Table 3), resulting in an enthalpy-driven association process promoted by H-bond/polar interactions. Contextually, for the alternative DAB/HSA ensemble, both ΔH_{b-ITC} and ΔS_{b-ITC} are positive, implying that interactions of hydrophobic nature are predominant in governing the binding between HSA and DAB. Moreover, the value of $T\Delta S_{b-ITC}$ for this complex ($+51.5$ kJ/mol = $(298$ K \times 172.8 J/(mol K)/1000); Table 3) is substantially larger than that of the corresponding ΔH_{b-ITC} , ultimately leading to a thermodynamically spontaneous (*i.e.*, $\Delta G_{b-ITC} < 0$) binding event.

Next, we determined the binding kinetics of DAB and VEM with HSA from the corresponding raw ITC data using the kinITC technology.^{20–23} KinITC complements ITC by analyzing the equilibration time of each injection during the titration and providing the association (k_{on}) and dissociation rate constants (k_{off}) for a 1:1 binding model, which are linked to the association constant K by

$$K_a = k_{on}/k_{off} \quad (7)$$

Accordingly, once K_a and k_{off} are determined *via* an ITC experiment, k_{on} can be calculated using eq 7, and finally, t_r is obtained as $1/k_{off}$ (see the sixth and seventh columns in Table 3). These data show that the ITC-derived values of k_{on} are very similar for the two drugs ($k_{on} = 1.57 \times 10^4$ and 1.12×10^4 M⁻¹ s⁻¹ for DAB and VEM, respectively), while a significant difference is observed in the k_{off} values (8.44×10^{-2} and 5.42×10^{-2} s⁻¹ for DAB and VEM, respectively), leading to a slightly higher residence time value VEM ($t_r = 18.5$ s) with respect to the alternative B-Raf inhibitor DAB ($t_r = 11.8$ s). These results are in line with the distinct thermodynamic binding profiles exhibited by the two anticancer drugs toward HSA: while strongly enthalpic interactions—like in the case of VEM/HSA—provide a more efficient contribution in fixing the ligand at the binding site, higher residual ligand mobility within the binding pocket—as it is the case of the DAB/HSA complex—although entropically beneficial results in interactions that are somewhat less efficient in maintaining the drug in its bound state.

In concluding this section, we observe here that in its role as a drug carrier, HSA may be able to promote drug delivery to the action site and may also be associated with drug safety concerns. It follows that the interaction of anticancer drugs with HSA is very important in oncology targeted therapies, especially in the case of highly plasma-bound compounds

(blood-free drug $<5\%$)—such as the B-Raf inhibitors DAB and VEM investigated in this study. Based on the free drug hypothesis, for a linear system, the unbound protein concentration P_f can be assumed constant and equal to the total protein concentration in plasma P_0 .⁸⁸ Accordingly, the unbound drug fraction D_f in plasma can be calculated as

$$D_f = 1/(1 + P_0/K_d) \quad (8)$$

where $K_d = 1/K_a = k_{off}/k_{on}$ (see eq 7). Substituting the expression of K_d in eq 8 yields

$$D_f = k_{off}/(k_{on}P_0 + k_{off}) \quad (9)$$

Since the average concentration of HSA in blood serum is $P_0 = 6 \times 10^{-4}$ M,¹¹ by inserting this value along with the k_{on} and k_{off} values derived in this work for DAB and VEM, respectively (Table 3), it is easily seen that the corresponding D_f values are 0.89 and 0.80%, respectively, in excellent agreement with the relevant clinical data ($<1\%$).

3.4. Resonance Energy-Transfer (RET) Interaction from HSA to DAB and VEM. Resonance energy transfer (RET, also known as fluorescence resonance energy transfer, FRET, or electronic energy transfer, EET) is an optical process in which an excited molecule—usually referred to as the donor—transfers its excess energy to an acceptor molecule.^{19,89,90} RET is based on the interaction of two kinds of fundamental particles: electrons and photons. Briefly, in RET, the surplus energy is transmitted to the acceptor in the form of the released virtual photon in RET when the electron relaxes to a lower-energy electronic state in the donor—this transfer is aided by dipole–dipole couplings between the molecules. The theoretical treatment of RET was refined by Förster,⁹¹ who discovered that energy transmission between molecules through dipole coupling is mostly determined by two factors: spectral overlap and intermolecular distance.⁹² For the rate of resonance energy transfer in the short range, the energy transfer yield E can be calculated as follows

$$E = 1 - F_{DA}/F_D = R_0^6/(R_0^6 + R^6) \quad (10)$$

where F_{DA} and F_D are the donor fluorescence intensities (here HSA) in the presence and absence of an acceptor (DAB or VEM), respectively, R is the distance between the donor and the acceptor, while R_0 (also known as the Förster critical distance) is a constant for each donor–acceptor pair and is defined as the distance at which energy transfer E is 50% efficient. R_0 can be computed as follows

$$R_0^6 = 8.8 \times 10^{23} \times k^2 \times n^{-4} \times \Phi_D \times J(\lambda) \quad (11)$$

where n denotes the refractive index of the medium in the wavelength range where there is considerable spectral overlap (here 1.336), Φ_D is the quantum yield of the donor (0.15 for

HSA), while the orientation of the donor and acceptor is described by k^2 , for which a commonly accepted value is 2/3 assuming random tumbling of the fluorophores. The degree of overlap between the donor and acceptor (as shown in Figure 4) may be used to determine the overlap integral $J(\lambda)$ in eq 10 according to

$$J(\lambda) = \int_0^\infty F(\lambda)\varepsilon(\lambda)\lambda^4 d\lambda / \int_0^\infty F(\lambda) d\lambda \quad (12)$$

in which $F(\lambda)$ is the donor's normalized fluorescence intensity at wavelength λ , and $\varepsilon(\lambda)$ is the acceptor's extinction coefficient at λ .

Therefore, the E , $J(\lambda)$, R_0 , and R values can be calculated according to eqs 10–12, and the relevant results are reported in Table 4.

Table 4. RET Parameters for the DAB/HSA and VEM/HSA Complexes

DAB/HSA				
E (%)	J (10^{-15} $\text{cm}^3 \text{L mol}^{-1}$)	R_0 (nm)	R (nm)	dynamic range (nm) ^a
13.1	1.19	1.79	2.46	0.895–2.68
VEM/HSA				
E (%)	J (10^{-15} $\text{cm}^3 \text{L mol}^{-1}$)	R_0 (nm)	R (nm)	dynamic range (nm)
15.6	0.905	1.71	2.27	0.855–2.56

^aThe dynamic range is defined as $0.5R_0 \leq R \leq 1.5R_0$. See the text for an explanation.

Before commenting on these data, it is important to recall here that the distance range (also called the dynamic range) that is accessible through reliable RET measurements is $\sim 0.5R_0 \leq R \leq 1.5R_0$.⁸⁰ In fact, if $R = 2 \times R_0$, the RET efficiency becomes <0.016 and thus negligible, where for $R = 0.5 \times R_0$, the RET efficiency becomes >0.984 .⁹³ As seen from the values listed in Table 4, the distance R between the protein donor W214 and the interacting drug (acceptor) is similar in both complexes (1.79 nm for DAB/HSA and 1.71 nm for VEM/HSA, respectively) and falls nicely within the corresponding dynamic ranges. This implies that RET from the protein donor to the two B-Raf inhibitors does occur with high probability and that the corresponding R values can be determined with good accuracy. Moreover, the fact that R is greater than R_0 for both systems can be taken as a further indication of the fact that a binding-related quenching mechanism is at play during HSA fluorescence quenching by these two anticancer drugs.

3.5. Structural Analysis of the DAB/HSA and VEM/HSA Complexes. **3.5.1. Circular Dichroism Spectroscopy.** To investigate the possible influence of DAB and VEM binding on the secondary structure of HSA, far-UV CD spectroscopy

measurements were performed on HSA alone and in the presence of each B-Raf inhibitor. As shown in Figure 5, the CD spectrum of pure HSA exhibits the two characteristic minima at 208 nm (arising from the exciton splitting of electronic transitions from the peptide amide nonbonding orbital π_{nb} to the antibonding orbital π^*) and 222 nm (arising from the electronic transition from an oxygen lone pair orbital n to the π^* orbital), respectively, which constitute the prototypical spectral signature of the α -helical structures of this protein.

Interestingly, upon the addition of increasing drug concentrations, the intensities of these bands for both DAB/HSA and VEM/HSA complexes exhibit only a very small increase with no discernible shift of the band minima, implying modest perturbations of the protein secondary structure upon ligand binding. To quantify these effects, we estimated the content of the α -helical motifs (% α -helix) for free HSA and in the presence of either B-Raf inhibitor at the three different molar ratios (0.5, 1, and 2) via the two well-known relationships

$$\text{MRE}_{208} = \text{observed ellipticity (mdeg)} / 10C_p n l \quad (13)$$

$$\% \alpha\text{-helix} = (-\text{MRE}_{208} - 4000 / 33\,000 - 4000) \times 100 \quad (14)$$

where MRE_{208} (expressed in $\text{deg cm}^2 \text{dmol}^{-1}$) is the observed mean residue ellipticity value at $\lambda = 208$ nm, $33000 \text{ deg cm}^2 \text{dmol}^{-1}$ and $4000 \text{ deg cm}^2 \text{dmol}^{-1}$ corresponds to the MRE_{208} values of pure α -helical and β -sheet/random coil structures, respectively, C_p is the protein concentration (in M), n is the number of amino acids in the protein (585 for HSA), and l is the path length of the cell (here 0.1 cm). The results confirm that, compared to free HSA (% α -helix = 58.0), binding of both anticancer drugs at 298 K induces only a very small perturbation even at the highest drug/protein molar ratio considered (% α -helix = 55.7 and 55.1% in the case of DAB and VEM, respectively). A very similar trend was observed at the other two temperature values investigated (data not shown). We also note that the α -helix contents estimated from our CD data are slightly lower than those derived from available HSA X-ray-derived crystal structures ($\sim 67\%$), although they are in line with other literature reports.^{60,64,94–98} This discrepancy can be attributed to several factors, including the use of different instruments and experimental conditions, as well as changes in the protein structural element in passing from a solid (X-ray diffraction) to a solution (CD spectroscopy) state.

3.5.2. Determination of the DAB and VEM Binding Site on HSA. Two well-defined binding sites, notably Sudlow's sites I and II (found in the HSA subdomains IIA and IIIA,

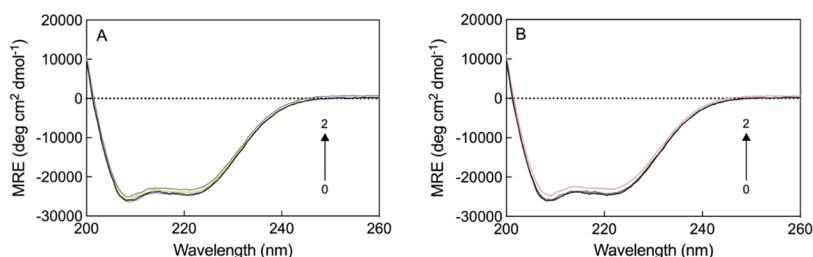


Figure 5. Far-UV CD spectra of HSA alone (0) and in the presence of DAB (A) and VEM (B) in a molar ratio of 0.5, 1, and 2 (PBS buffer, pH = 7.4, $T = 298$ K, $[\text{HSA}] = 2 \mu\text{M}$).

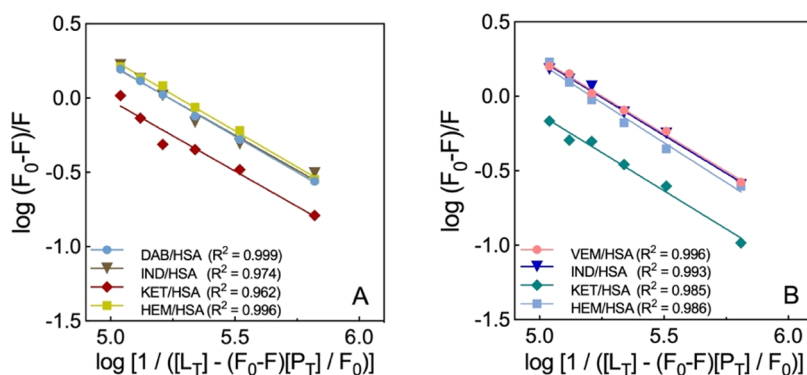


Figure 6. Plots of $\log(F_0 - F)$ vs $\log[1/([L_T] - (F_0 - F)[P_T]/F_0)]$ for the fluorescence quenching of HSA ($2 \mu\text{M}$) by DAB (A) and VEM (B) at different concentrations ($1-6 \mu\text{M}$) in the presence of the three site markers IND, KET, and HEM [$2 \mu\text{M}$] at 298 K (PBS, pH = 7.4).

respectively), have been classified as having a high affinity for a wide range of different drugs.^{99–102} In addition, another binding pocket, known as drug binding site III and located in the HSA subdomain IB, has been reported.¹⁰³ To probe which of these three protein regions could constitute potential binding site(s) for DAB and VEM on HSA, we next carried out site displacement studies. Purposely, we selected three drugs with known binding sites on HSA—*i.e.*, indomethacin (IND), ketoprofen (KET), and hemin (HEM)—as specific site markers for binding sites I, II, and III, respectively,^{20,21} and recorded the fluorescence emission spectra obtained upon titration of premixed solutions of HSA and each site marker with progressively increasing concentrations of the two B-Raf inhibitors. Data fitting through eq 3 (Figure 6) allowed us to quantify the effect of the presence of each site marker on the HSA binding of DAB and VEM via the determination of the relevant binding constant K_a , as shown in Table 5.

Table 5. Binding Constants for DAB and VEM on HSA Derived from Fluorescence Quenching Data Obtained at 298 K in the Absence and Presence of the Three Site Markers IND, KET, and MET Using Equation 3

site marker	K_a (10^5 M^{-1})	site marker	K_a (10^5 M^{-1})
none	1.72 ± 0.03	none	1.74 ± 0.03
IND	1.58 ± 0.05	IND	1.71 ± 0.03
KET	0.586 ± 0.08	KET	0.926 ± 0.07
HEM	1.65 ± 0.03	HEM	1.61 ± 0.06

As we see from Table 5, the affinity of both DAB and VEM for HSA in the presence of KET is substantially lower compared to that of HSA alone, while their K_a values are essentially unaffected in the presence of the two alternative site markers IND and HEM. In aggregate, these data support the displacement interaction between the two B-Raf inhibitors and KET in HSA binding, thereby indicating Sudlow’s binding site II in the HSA subdomain IIIA as the putative DAB and VEM binding pockets on the protein.

3.5.3. Molecular Simulations of the DAB and VEM in Complex with HSA. To gain further structural information on the interactions between DAB and VEM with HSA, we exploited the information gathered by the competition experiments discussed above to perform molecular dynamics (MD) simulations of the two anticancer drugs within the protein subdomain IIIA (Figure 7). Molecular docking was used to arrange the two B-Raf inhibitors inside the experimentally recognized binding pocket. For both DAB

and VEM, the most favorable conformation identified by the docking algorithm was carried on to the subsequent MD simulations. Specifically, the calculated docking scoring energies for the selected pose were -35.15 and -35.98 kJ/mol for DAB/HSA and for VEM/HSA complexes, respectively. These values are in good agreement with the albumin affinity trend obtained from the experimental techniques. Given that the intrinsic limitations of the docking procedure are out of the scope of this work to speculate on the docking energy and its component values, but rather we want to exploit the computational approach to qualitatively describe the binding mechanism and kinetics of the two B-Raf inhibitors toward HSA. Starting the analysis with the DAB/HSA complex (left panel in Figure 7), during the corresponding unrestrained MD run, the 2-6-difluorobenzene ring of the drug remains well located in a deep hydrophobic pocket lined by the side chains of HSA residues L387, I388, L407, L430, V433, L453, L457, and Y411. The guanidinium group of R410 stabilizes the outermost portion of DAB sharing a polar interaction with the sulfur atom of the drug thiazole moiety. Another weak polar interaction is stably detected between the side chain of N391 and the $-\text{NH}_2$ group of the DAB pyrimidin-2-amino group; the latter is further stabilized by hydrophobic contacts with the side chains of L394 and F403 and the aliphatic portion of R410. In agreement with the experimental binding thermodynamics data derived from both fluorescence spectroscopy and ITC (Tables 2 and 3), a network of hydrophobic forces mainly characterizes the interactions between DAB and HSA, resulting in an essentially entropy-driven binding process. Notably, the average distance of DAB from HSA W214 is 2.37 nm, in agreement with the R value determined by RET calculations (Table 4), further confirming the anticancer drug binding location and mode within Sudlow’s site II, subdomain IIIA of the protein.

The analysis of the equilibrated portion of the MD trajectory of the alternative VEM/HSA complex reveals that the chlorobenzene ring of VEM is inserted in a hydrophobic region formed by the side chains of HSA residues L387, I388, L407, L430, V433, L453, and F403. Interestingly, two permanent hydrogen bonds (HBs) are also detected that further contribute to the relevant complex stabilization. In detail, the side-chain $-\text{OH}$ group of S489 is engaged in a HB with the N atom of the VEM condensed pyrrole ring (average dynamic length (ADL) = $2.95 \pm 0.15 \text{ \AA}$), while the ϵ -amino group of K414 establishes a HB with one of the O atoms of the VEM sulfone moiety (ADL = $3.02 \pm 0.15 \text{ \AA}$). Moreover, the side chains of HSA residues F488, Y411, and R410 originate

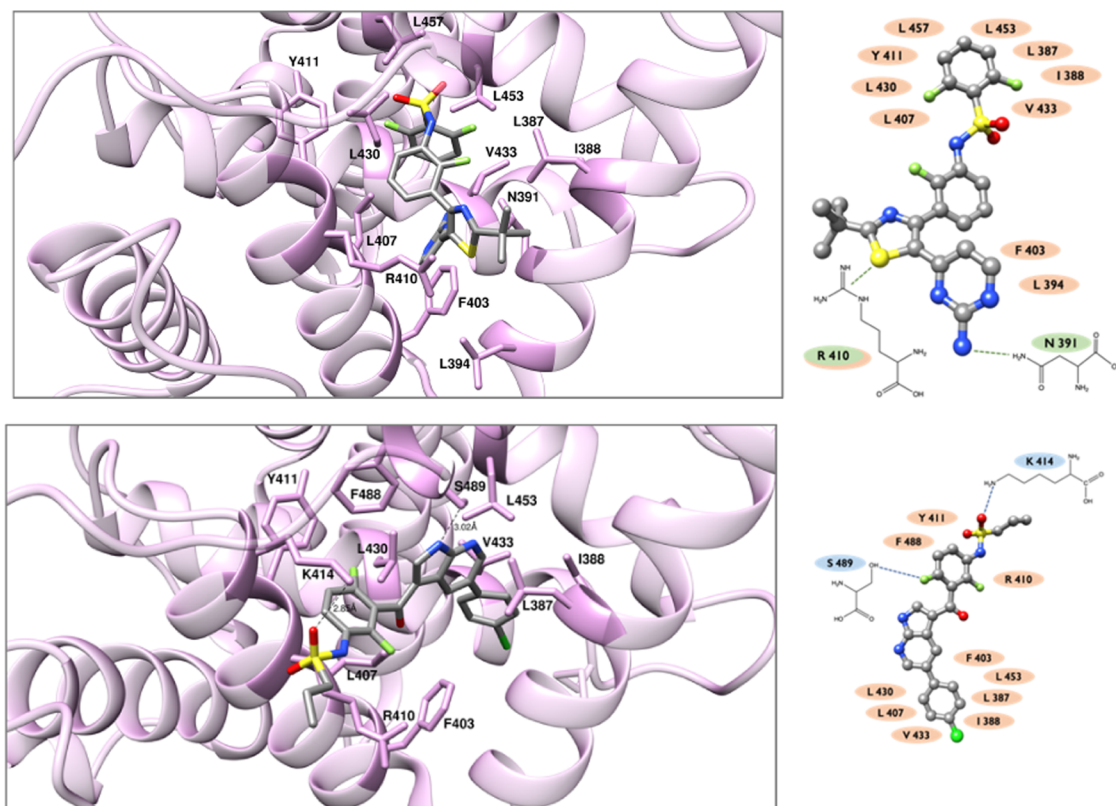


Figure 7. Binding of DAB (upper panels) and VEM (lower panels) in Sudlow's site II (subdomain IIIA) of HSA. (Left panels) Representative snapshot extracted from the relevant MD simulations. The protein is shown in mulberry ribbons, while the two B-Raf inhibitors are depicted as atom-colored sticks (C, gray; O, red; N, blue; S, yellow; F, light green; Cl, forest green). HSA residues mainly involved in drug binding are highlighted and labeled. Hydrogen bonds (HBs) are indicated by broken black lines and labeled. Hydrogen atoms, water molecules, ions, and counterions are not shown for clarity. (Right panels) Schematic representation of the HSA amino acids mostly involved in the binding site, as highlighted from the corresponding MD simulations. The two B-Raf inhibitors are depicted as balls and sticks and colored by elements. Hydrogen atoms are not shown for clarity. The HSA residues involved in hydrogen bonds or polar interactions are represented in light blue and light green, respectively, and the dashed lines are used to represent the corresponding interaction. Residues involved in hydrophobic interactions are depicted in light pink.

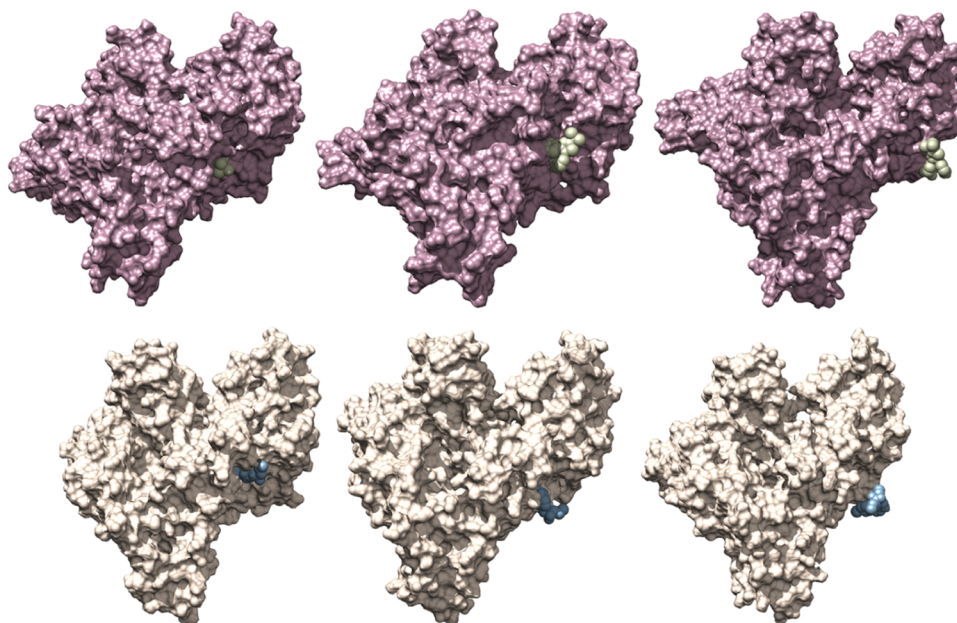


Figure 8. Snapshots extracted from the trajectories of the frequency adaptive metadynamics (FaMetaD) simulations showing DAB (top panel, lint spheres) and VEM (bottom panel, dusk blue spheres) leaving their binding sites on HSA (represented via its van der Waals surface colored in orchid haze and mother of pearl, respectively).

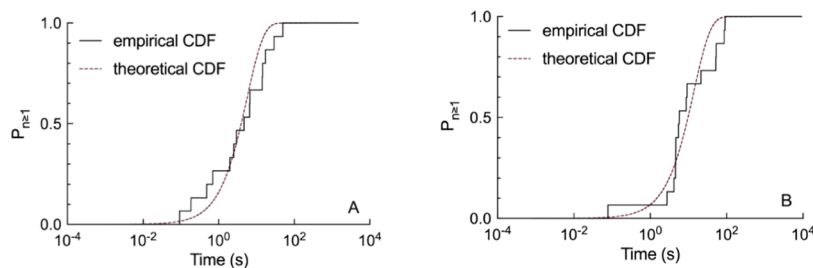


Figure 9. Least-squares fitting of the empirical cumulative distribution function (CDF_E) of the unbiased release times obtained from the FaMetaD simulations of the DAB/HSA (A) and VEM/HSA (B) systems with the theoretical expression of the cumulative distribution function (CDF_T) for a homogeneous Poisson process.

from another hydrophobic environment, which encases the 2-6-difluorobenzene portion of this B-Raf inhibitor. This VEM binding mode to HSA within the protein Sudlow’s site II (subdomain IIIA) not only well explains the largely enthalpic contribution to the corresponding complex formation derived from combined fluorescence- and ITC-based experiments discussed above (Tables 2 and 3) but also provides information about the existence of two important intermolecular HBs, which could not be probed directly by any of the experimental techniques adopted. Furthermore, the average distance of VEM from HSA W214 (2.18 nm) also nicely matches the R value estimated by RET (Table 4), yielding additional support to the VEM/HSA binding mode predicted by molecular simulations.

Finally, molecular simulations were further exploited to derive the residence time t_r of the two anticancer drugs DAB and VEM within the HSA binding site. Through the adoption of the frequency adaptive metadynamics (FaMetaD) approach,⁴² it is possible to bias the simulations to observe, in reasonable computation times, rare events like drug dissociation from their binding site, as exemplified in Figure 8 by the present results obtained for the DAB/HSA and VEM/HSA systems.

According to the method, a history-dependent biasing potential on the relevant reaction coordinates is added on a regular basis, flattening the energy surface to accelerate the occurrence of rare events such as those presently under investigation, and the simulation is ended when the unbinding is observed. An acceleration factor, dependent on the temporal biasing potential deposited during FaMetaD, can be recorded during the FaMetaD simulation and can then be used to retrieve the unbiased drug release time simply by multiplying it by the biased time needed to observe the unbinding event. Through different independent FaMetaD simulations (15 simulation runs were performed for either VEM or DAB bound to HSA), the mean value of the drug t_r can then be retrieved as the characteristic transition time of a homogeneous Poisson process (τ).⁴⁶ To the purpose, the empirical cumulative distribution function (CDF_E) of the unbiased release times obtained from FaMetaD was least-squares-fitted with the theoretical expression of the cumulative distribution function (CDF_T) for a homogeneous Poisson process (shown in Figure 9) given by the equation

$$CDF_T = 1 - e^{-t/\tau} \quad (15)$$

In addition, through a Kolmogorov–Smirnov test, it is possible to compare the CDF_E and CDF_T , obtaining an estimation of the quality of the collected data in the form of a p -value, which must be greater than 0.05. The obtained p -

values were 0.292 and 0.261 for VEM and DAB, respectively. The t_r values for VEM and DAB obtained from these FaMetaD simulations are 5.73 ± 2.5 and 14.0 ± 6.1 s, respectively (see the last column of Table 3). These values, as already mentioned in Section 3.3, are in very good agreement with those experimentally determined through kinITC experiments, with the B-Raf inhibitor VEM being characterized by a sensibly greater t_r value with respect to DAB, in line with the different networks of interactions underlying the two anticancer drugs to HSA.

4. CONCLUSIONS

In this work, we exploited a combined approach based on experimental and molecular simulation techniques to investigate the binding process of two clinically approved anticancer drugs, dabrafenib and vemurafenib, to human serum albumin. In aggregate, the results show that both DAB and VEM bind within the protein Sudlow’s site II, subdomain IIIA with comparable affinities and without causing significant perturbations of the protein’s secondary structure yet with an opposite mechanism. Indeed, DAB associates with HSA *via* an entropy-driven mechanism largely promoted by a set of hydrophobic interactions. In contrast, the nature of the VEM/HSA association is mainly enthalpic due to the establishment of two permanent intermolecular HBs along with further stabilizing nonpolar interactions. In line with this, VEM has a somewhat smaller dissociation rate constant—and hence a slightly greater residence time within the protein binding site—with respect to DAB, as k_{off} (and hence $t_r = 1/k_{off}$) is strongly dependent on the nature of interactions in the bound state. Generally, when a few isolated strong connections between chemical groups of the ligand and protein exist, they form a single considerable activation barrier to ligand release, which is seldom passed since a sufficient quantity of energy is rarely available. Consequently, the k_{off} value of a given drug in such situations will be small while the time it will spend in contact with its biological target, thereby exerting its pharmacological activity, will be large. In contrast, if there are many weak interactions stabilizing a given ligand/protein complex, each of these can be broken successively with relatively small amounts of energy. When this is the case, the drug k_{off} value will be large, which will translate into a short drug residence time and, hence, diminished activity at its target. Finally, the data provided in this study give precise information regarding the binding properties to HSA of two anticancer treatments being used in clinics to treat melanoma, which may contribute to further understanding of their mode of action and pharmacokinetic features.

■ ASSOCIATED CONTENT

● Supporting Information:

Fluorescence spectrum of HSA in the presence of ethanol and fluorescence spectra of VEM and DAB alone ([PDF](#))

■ AUTHOR INFORMATION

Corresponding Author

Erik Laurini – Molecular Biology and Nanotechnology
Laboratory (MolBNL@UniTS), DEA, University of Trieste,
34127 Trieste, Italy; orcid.org/0000-0001-6092-6532;
Email: erik.laurini@dia.units.it

Authors

Maria Russi – Molecular Biology and Nanotechnology
Laboratory (MolBNL@UniTS), DEA, University of Trieste,
34127 Trieste, Italy

Gabriele Cavalieri – Molecular Biology and Nanotechnology
Laboratory (MolBNL@UniTS), DEA, University of Trieste,
34127 Trieste, Italy

Domenico Marson – Molecular Biology and Nanotechnology
Laboratory (MolBNL@UniTS), DEA, University of Trieste,
34127 Trieste, Italy

Sabrina Pricl – Molecular Biology and Nanotechnology
Laboratory (MolBNL@UniTS), DEA, University of Trieste,
34127 Trieste, Italy; Department of General Biophysics,
Faculty of Biology and Environmental Protection, University
of Lodz, 90-236 Łódź, Poland

Author Contributions

E.L. and S.P. designed the research. M.R. and G.C. performed all experiments and collected/organized all experimental data. D.M. performed the molecular simulations. M.R., D.M., E.L., and S.P. performed all data analysis. S.P. and E.L. supervised the research, and S.P. and E.L. wrote the manuscript. All authors contributed and agreed to the final version of the manuscript.

Notes

The authors declare no competing financial interest.
The data that support the findings of this study are included in this published article.

■ ACKNOWLEDGMENTS

The authors wish to acknowledge the generous financial support from the Italian Association for Cancer Research (AIRC, grant “Novel hot-spot mutations in BCR-ABL1: role in resistance to CML target therapy—IG17413” to S.P.), the Friuli Venezia Giulia Region (REFVG, grant “Study of the oncogene B-Raf and its mutation for the selection of melanoma patients eligible for targeted therapies with specific inhibitors—No-Mel” to S.P.), and the Fondazione Cassa di Risparmio di Trieste (Fondazione CRTrieste, grant “Far-UV CD spectroscopy in translational medicine” to S.P.).

■ REFERENCES

- (1) Djavid, A. R.; Stonesifer, C.; Fullerton, B. T.; Wang, S. W.; Tartaro, M. A.; Kwinta, B. D.; Grimes, J. M.; Geskin, L. J.; Saenger, Y. M. Etiologies of Melanoma Development and Prevention Measures: A Review of the Current Evidence. *Cancers* **2021**, *13*, No. 4914.
- (2) Michielin, O.; van Akkooi, A. C. J.; Ascierto, P. A.; Dummer, R.; Keilholz, U. Cutaneous melanoma: ESMO Clinical Practice Guidelines for diagnosis, treatment and follow-up†. *Ann. Oncol.* **2019**, *30*, 1884–1901.
- (3) Miller, R.; Walker, S.; Shui, I.; Brandtmüller, A.; Cadwell, K.; Scherrer, E. Epidemiology and survival outcomes in stages II and III cutaneous melanoma: a systematic review. *Melanoma Manage* **2020**, *7*, No. MMT39.
- (4) Sandru, A.; Voinea, S.; Panaitescu, E.; Blidaru, A. Survival rates of patients with metastatic malignant melanoma. *J. Med. Life* **2014**, *7*, 572–576.
- (5) Dhillon, A. S.; Hagan, S.; Rath, O.; Kolch, W. MAP kinase signalling pathways in cancer. *Oncogene* **2007**, *26*, 3279–3290.
- (6) Dankner, M.; Rose, A. A. N.; Rajkumar, S.; Siegel, P. M.; Watson, I. R. Classifying BRAF alterations in cancer: new rational therapeutic strategies for actionable mutations. *Oncogene* **2018**, *37*, 3183–3199.
- (7) Rheault, T. R.; Stellwagen, J. C.; Adjabeng, G. M.; Hornberger, K. R.; Petrov, K. G.; Waterson, A. G.; Dickerson, S. H.; Mook, R. A.; Laquerre, S. G.; King, A. J.; Rossanese, O. W.; Arnone, M. R.; Smitheman, K. N.; Kane-Carson, L. S.; Han, C.; Moorthy, G. S.; Moss, K. G.; Uehling, D. E. Discovery of Dabrafenib: A Selective Inhibitor of Raf Kinases with Antitumor Activity against B-Raf-Driven Tumors. *ACS Med. Chem. Lett.* **2013**, *4*, 358–362.
- (8) Goyal, G.; Heaney, M. L.; Collin, M.; Cohen-Aubart, F.; Vaglio, A.; Durham, B. H.; Hershkovitz-Rokah, O.; Girschikofsky, M.; Jacobsen, E. D.; Toyama, K.; Goodman, A. M.; Hendrie, P.; Cao, X. X.; Estrada-Veras, J. I.; Shpilberg, O.; Abdo, A.; Kurokawa, M.; Dagna, L.; McClain, K. L.; Mazor, R. D.; Picarsic, J.; Janku, F.; Go, R. S.; Haroche, J.; Diamond, E. L. Erdheim-Chester disease: consensus recommendations for evaluation, diagnosis, and treatment in the molecular era. *Blood* **2020**, *135*, 1929–1945.
- (9) Roberts, J. A.; Pea, F.; Lipman, J. The clinical relevance of plasma protein binding changes. *Clin. Pharmacokinet.* **2013**, *52*, 1–8.
- (10) Muller, P. Y.; Milton, M. N. The determination and interpretation of the therapeutic index in drug development. *Nat. Rev. Drug Discovery* **2012**, *11*, 751–761.
- (11) Peters, T. *All About Albumin: Biochemistry, Genetics, and Medical Applications*; Academic Press: San Diego, CA, 1995.
- (12) Fanali, G.; di Masi, A.; Trezza, V.; Marino, M.; Fasano, M.; Ascenzi, P. Human serum albumin: from bench to bedside. *Mol. Aspects Med.* **2012**, *33*, 209–290.
- (13) Sharifi-Rad, A.; Mehrzad, J.; Darroudi, M.; Saberi, M. R.; Chamani, J. Oil-in-water nanoemulsions comprising Berberine in olive oil: biological activities, binding mechanisms to human serum albumin or holo-transferrin and QMMD simulations. *J. Biomol. Struct. Dyn.* **2021**, *39*, 1029–1043.
- (14) Merlot, A. M.; Kalinowski, D. S.; Richardson, D. R. Unraveling the mysteries of serum albumin—more than just a serum protein. *Front. Physiol.* **2014**, *5*, No. 299.
- (15) Rabbani, G.; Ahn, S. N. Structure, enzymatic activities, glycation and therapeutic potential of human serum albumin: A natural cargo. *Int. J. Biol. Macromol.* **2019**, *123*, 979–990.
- (16) Evans, T. W. Review article: albumin as a drug—biological effects of albumin unrelated to oncotic pressure. *Aliment. Pharmacol. Ther.* **2002**, *16*, 6–11.
- (17) Pace, C. N.; Vajdos, F.; Fee, L.; Grimsley, G.; Gray, T. How to measure and predict the molar absorption coefficient of a protein. *Protein Sci.* **1995**, *4*, 2411–2423.
- (18) Leggio, C.; Galantini, L.; Pavel, N. V. About the albumin structure in solution: cigar expanded form versus heart normal shape. *Phys. Chem. Chem. Phys.* **2008**, *10*, 6741–6750.
- (19) Lakowicz, J. R. *Principles of Fluorescence Spectroscopy*, 3rd ed.; Springer: New York, 2006.
- (20) Zhivkova, Z. D. Studies on drug-human serum albumin binding: the current state of the matter. *Curr. Pharm. Des.* **2015**, *21*, 1817–1830.

- (21) Zunszain, P. A.; Ghuman, J.; Komatsu, T.; Tsuchida, E.; Curry, S. Crystal structural analysis of human serum albumin complexed with hemin and fatty acid. *BMC Struct. Biol.* **2003**, *3*, No. 6.
- (22) Burnouf, D.; Ennifar, E.; Guedich, S.; Puffer, B.; Hoffmann, G.; Bec, G.; Disdier, F.; Baltzinger, M.; Dumas, P. kinITC: A New Method for Obtaining Joint Thermodynamic and Kinetic Data by Isothermal Titration Calorimetry. *J. Am. Chem. Soc.* **2012**, *134*, 559–565.
- (23) Zihlmann, P.; Silbermann, M.; Sharpe, T.; Jiang, X.; Mülthaler, T.; Jakob, R. P.; Rabbani, S.; Sager, C. P.; Frei, P.; Pang, L.; Maier, T.; Ernst, B. KinITC-One Method Supports both Thermodynamic and Kinetic SARs as Exemplified on FimH Antagonists. *Chemistry* **2018**, *24*, 13049–13057.
- (24) Dumas, P.; Ennifar, E.; Da Veiga, C.; Bec, G.; Palau, W.; Di Primo, C.; Piñeiro, A.; Sabin, J.; Muñoz, E.; Rial, J. Extending ITC to Kinetics with kinITC. In *Methods in Enzymology*; Feig, A. L., Ed.; Academic Press, 2016; Chapter 7, Vol. 567, pp 157–180.
- (25) Glöckner, S.; Klebe, G. Simultaneous determination of thermodynamic and kinetic data by isothermal titration calorimetry. *Biochim. Biophys. Acta, Gen. Subj.* **2021**, *1865*, No. 129772.
- (26) Berman, H. M.; Westbrook, J.; Feng, Z.; Gilliland, G.; Bhat, T. N.; Weissig, H.; Shindyalov, I. N.; Bourne, P. E. The Protein Data Bank. *Nucleic Acids Res.* **2000**, *28*, 235–242.
- (27) Wang, Y.; Yu, H.; Shi, X.; Luo, Z.; Lin, D.; Huang, M. Structural mechanism of ring-opening reaction of glucose by human serum albumin. *J. Biol. Chem.* **2013**, *288*, 15980–15987.
- (28) Anandakrishnan, R.; Aguilar, B.; Onufriev, A. V. H++ 3.0: automating pK prediction and the preparation of biomolecular structures for atomistic molecular modeling and simulations. *Nucleic Acids Res.* **2012**, *40*, W537–W541.
- (29) Hanwell, M. D.; Curtis, D. E.; Lonie, D. C.; Vandermeersch, T.; Zurek, E.; Hutchison, G. R. Avogadro: an advanced semantic chemical editor, visualization, and analysis platform. *J. Cheminf.* **2012**, *4*, No. 17.
- (30) Wang, J.; Romain, M. W.; James, W. C.; Peter, A. K.; David, A. C. Development and testing of a general amber force field. *J. Comput. Chem.* **2004**, *25*, 1157–1174.
- (31) Case, D.A.; Belfon, K.; Ben-Shalom, I. Y.; Brozell, S. R.; Cerutti, D. S.; Cheatham, T. E., III; Cruzeiro, V.W.D.; Darden, T. A.; Duke, R. E.; Giambasu, G.; Gilson, M. K.; Gohlke, H.; Goetz, A. W.; Harris, R.; Izadi, S.; Izmailov, S. A.; Kasavajhala, K.; Kovalenko, A.; Krasny, R.; Kurtzman, T.; Lee, T. S.; LeGrand, S.; Li, P.; Lin, C.; Liu, J.; Luchko, T.; Luo, R.; Man, V.; Merz, K. M.; Miao, Y.; Mikhailovskii, O.; Monard, G.; Nguyen, H.; Onufriev, A.; Pan, F.; Pantano, S.; Qi, R.; Roe, D. R.; Roitberg, A.; Sagui, C.; Schott-Verdugo, S.; Shen, J.; Simmerling, C.; Skrynnikov, N. R.; Smith, J.; Swails, J.; Walker, R. C.; Wang, J.; Wilson, L.; Wolf, R. M.; Wu, X.; Xiong, Y.; Xue, Y.; York, D. M.; Kollman, P. A. *AMBER 2020*; University of California: San Francisco, 2020.
- (32) Vanquelef, E.; Simon, S.; Marquant, G.; Garcia, E.; Klimerak, G.; Delepine, J. C.; Cieplak, P.; Dupradeau, F.-Y. R.E.D. Server: a web service for deriving RESP and ESP charges and building force field libraries for new molecules and molecular fragments. *Nucleic Acids Res.* **2011**, *39*, W511–W517.
- (33) Dupradeau, F.-Y.; Pigache, A.; Zaffran, T.; Savineau, C.; Lelong, R.; Grivel, N.; Lelong, D.; Rosanski, W.; Cieplak, P. The R.E.D. tools: advances in RESP and ESP charge derivation and force field library building. *Phys. Chem. Chem. Phys.* **2010**, *12*, 7821–7839.
- (34) Maier, J. A.; Martinez, C.; Kasavajhala, K.; Wickstrom, L.; Hauser, K. E.; Simmerling, C. ff14SB: Improving the Accuracy of Protein Side Chain and Backbone Parameters from ff99SB. *J. Chem. Theory Comput.* **2015**, *11*, 3696–3713.
- (35) Jorgensen, W. L.; Chandrasekhar, J.; Madura, J. D.; Impey, R. W.; Klein, M. L. Comparison of simple potential functions for simulating liquid water. *J. Chem. Phys.* **1983**, *79*, 926–935.
- (36) Berendsen, H. J. C.; Postma, J. P. M.; van Gunsteren, W. F.; DiNola, A.; Haak, J. R. Molecular dynamics with coupling to an external bath. *J. Chem. Phys.* **1984**, *81*, 3684–3690.
- (37) Toukmaji, A.; Sagui, C.; Board, J.; Darden, T. Efficient particle-mesh Ewald based approach to fixed and induced dipolar interactions. *J. Chem. Phys.* **2000**, *113*, 10913–10927.
- (38) Loncharich, R. J.; Brooks, B. R.; Pastor, R. W. Langevin dynamics of peptides: the frictional dependence of isomerization rates of N-acetylalanine-N'-methylamide. *Biopolymers* **1992**, *32*, 523–535.
- (39) Ryckaert, J.-P.; Ciccotti, G.; Berendsen, H. J. C. Numerical integration of the cartesian equations of motion of a system with constraints: molecular dynamics of n-alkanes. *J. Comput. Phys.* **1977**, *23*, 327–341.
- (40) Trott, O.; Olson, A. J. AutoDock Vina: improving the speed and accuracy of docking with a new scoring function, efficient optimization, and multithreading. *J. Comput. Chem.* **2010**, *31*, 455–461.
- (41) Pettersen, E. F.; Goddard, T. D.; Huang, C. C.; Couch, G. S.; Greenblatt, D. M.; Meng, E. C.; Ferrin, T. E. UCSF Chimera—a visualization system for exploratory research and analysis. *J. Comput. Chem.* **2004**, *25*, 1605–1612.
- (42) Wang, Y.; Valsson, O.; Tiwary, P.; Parrinello, M.; Lindorff-Larsen, K. Frequency adaptive metadynamics for the calculation of rare-event kinetics. *J. Chem. Phys.* **2018**, *149*, No. 072309.
- (43) Tiwary, P.; Parrinello, M. From metadynamics to dynamics. *Phys. Rev. Lett.* **2013**, *111*, No. 230602.
- (44) The PLUMED consortium. Promoting transparency and reproducibility in enhanced molecular simulations. *Nat. Methods* **2019**, *16*, 670–673.
- (45) Tribello, G. A.; Bonomi, M.; Branduardi, D.; Camilloni, C.; Bussi, G. PLUMED 2: New feathers for an old bird. *Comput. Phys. Commun.* **2014**, *185*, 604–613.
- (46) Salvalaglio, M.; Tiwary, P.; Parrinello, M. Assessing the Reliability of the Dynamics Reconstructed from Metadynamics. *J. Chem. Theory Comput.* **2014**, *10*, 1420–1425.
- (47) Hellmann, N.; Schneider, D. Hands On: Using Tryptophan Fluorescence Spectroscopy to Study Protein Structure. *Methods in Molecular Biology*; Springer, 2019; Vol. 1958, pp 379–401.
- (48) Ding, Y.; Wang, H.; Zhang, L.; Li, L.; Zhang, H. Albumin-binding difference caused by hydroxy and bromo on position-2 of benzothiazole. *J. Mol. Liq.* **2021**, *337*, No. 116570.
- (49) Wu, D.; Tang, L.; Duan, R.; Hu, X.; Geng, F.; Zhang, Y.; Peng, L.; Li, H. Interaction mechanisms and structure-affinity relationships between hyperoside and soybean β -conglycinin and glycinin. *Food Chem.* **2021**, *347*, No. 129052.
- (50) Wu, D.; Duan, R.; Tang, L.; Zhou, D.; Zeng, Z.; Wu, W.; Hu, J.; Sun, Q. In-vitro binding analysis and inhibitory effect of capsaicin on lipase. *LWT* **2022**, *154*, No. 112674.
- (51) Zare-Feizabadi, N.; Amiri-Tehranizadeh, Z.; Sharifi-Rad, A.; Mokaberi, P.; Nosrati, N.; Hashemzadeh, F.; Rahimi, H. R.; Saberi, M. R.; Chamani, J. Determining the Interaction Behavior of Calf Thymus DNA with Anastazole in the Presence of Histone H1: Spectroscopies and Cell Viability of MCF-7 Cell Line Investigations. *DNA Cell Biol.* **2021**, *40*, 1039–1051.
- (52) Rabbani, G.; Lee, E. J.; Ahmad, K.; Baig, M. H.; Choi, I. Binding of Tolperisone Hydrochloride with Human Serum Albumin: Effects on the Conformation, Thermodynamics, and Activity of HSA. *Mol. Pharmaceutics* **2018**, *15*, 1445–1456.
- (53) Wu, D.; Duan, R.; Tang, L.; Hu, X.; Geng, F.; Sun, Q.; Zhang, Y.; Li, H. Binding mechanism and functional evaluation of quercetin 3-rhamnoside on lipase. *Food Chem.* **2021**, *359*, No. 129960.
- (54) Rabbani, G.; Baig, M. H.; Jan, A. T.; Ju Lee, E.; Khan, M. V.; Zaman, M.; Farouk, A. E.; Khan, R. H.; Choi, I. Binding of erucic acid with human serum albumin using a spectroscopic and molecular docking study. *Int. J. Biol. Macromol.* **2017**, *105*, 1572–1580.
- (55) Sułkowska, A. Interaction of drugs with bovine and human serum albumin. *J. Mol. Struct.* **2002**, *614*, 227–232.
- (56) Tayyab, S.; Izzudin, M. M.; Kabir, M. Z.; Feroz, S. R.; Tee, W. V.; Mohamad, S. B.; Alias, Z. Binding of an anticancer drug, axitinib to human serum albumin: Fluorescence quenching and molecular docking study. *J. Photochem. Photobiol., B* **2016**, *162*, 386–394.

- (57) Kabir, M. Z.; Mukarram, A. K.; Mohamad, S. B.; Alias, Z.; Tayyab, S. Characterization of the binding of an anticancer drug, lapatinib to human serum albumin. *J. Photochem. Photobiol., B* **2016**, *160*, 229–239.
- (58) Suo, Z.; Xiong, X.; Sun, Q.; Zhao, L.; Tang, P.; Hou, Q.; Zhang, Y.; Wu, D.; Li, H. Investigation on the Interaction of Dabrafenib with Human Serum Albumin Using Combined Experiment and Molecular Dynamics Simulation: Exploring the Binding Mechanism, Esterase-like Activity, and Antioxidant Activity. *Mol. Pharmaceutics* **2018**, *15*, 5637–5645.
- (59) Kabir, M. Z.; Tee, W. V.; Mohamad, S. B.; Alias, Z.; Tayyab, S. Comprehensive insight into the binding of sunitinib, a multi-targeted anticancer drug to human serum albumin. *Spectrochim. Acta, Part A* **2017**, *181*, 254–263.
- (60) Suo, Z.; Sun, Q.; Yang, H.; Tang, P.; Gan, R.; Xiong, X.; Li, H. Combined spectroscopy methods and molecular simulations for the binding properties of trametinib to human serum albumin. *RSC Adv.* **2018**, *8*, 4742–4749.
- (61) Liu, C.; Liu, Z.; Wang, J. Uncovering the molecular and physiological processes of anticancer leads binding human serum albumin: A physical insight into drug efficacy. *PLoS One* **2017**, *12*, No. e0176208.
- (62) Callis, P. R. Binding phenomena and fluorescence quenching. I: Descriptive quantum principles of fluorescence quenching using a supermolecule approach. *J. Mol. Struct.* **2014**, *1077*, 14–21.
- (63) Laurini, E.; Marson, D.; Posocco, P.; Fermeglia, M.; Pricl, S. Structure and binding thermodynamics of viologen-phosphorous dendrimers to human serum albumin: A combined computational/experimental investigation. *Fluid Phase Equilib.* **2016**, *422*, 18–31.
- (64) Yeggoni, D. P.; Rachamalla, A.; Subramanyam, R. A comparative binding mechanism between human serum albumin and α -1-acid glycoprotein with corilagin: biophysical and computational approach. *RSC Adv.* **2016**, *6*, 40225–40237.
- (65) Zolfaghazadeh, M.; Pirouzi, M.; Asoodeh, A.; Saberi, M. R.; Chamani, J. A comparison investigation of DNP-binding effects to HSA and HTF by spectroscopic and molecular modeling techniques. *J. Biomol. Struct. Dyn.* **2014**, *32*, 1936–1952.
- (66) Tayeh, N.; Rungassamy, T.; Albani, J. R. Fluorescence spectral resolution of tryptophan residues in bovine and human serum albumins. *J. Pharm. Biomed. Anal.* **2009**, *50*, 107–116.
- (67) Rahnama, E.; Mahmoodian-Moghaddam, M.; Khorsand-Ahmadi, S.; Saberi, M. R.; Chamani, J. Binding site identification of metformin to human serum albumin and glycated human serum albumin by spectroscopic and molecular modeling techniques: a comparison study. *J. Biomol. Struct. Dyn.* **2015**, *33*, 513–533.
- (68) Abou-Zied, O. K.; Al-Shihi, O. I. K. Characterization of Subdomain IIA Binding Site of Human Serum Albumin in its Native, Unfolded, and Refolded States Using Small Molecular Probes. *J. Am. Chem. Soc.* **2008**, *130*, 10793–10801.
- (69) Ware, W. R. Oxygen quenching of fluorescence in solution: an experimental study of the diffusion process. *J. Phys. Chem. A* **1962**, *66*, 455–458.
- (70) Bi, S.; Ding, L.; Tian, Y.; Song, D.; Zhou, X.; Liu, X.; Zhang, H. Investigation of the interaction between flavonoids and human serum albumin. *J. Mol. Struct.* **2004**, *703*, 37–45.
- (71) Ross, P. D.; Subramanian, S. Thermodynamics of protein association reactions: forces contributing to stability. *Biochemistry* **1981**, *20*, 3096–3102.
- (72) Renaud, J. P.; Chung, C. W.; Danielson, U. H.; Egner, U.; Hennig, M.; Hubbard, R. E.; Nar, H. Biophysics in drug discovery: impact, challenges and opportunities. *Nat. Rev. Drug Discovery* **2016**, *15*, 679–698.
- (73) Falconer, R. J.; Schuur, B.; Mittermaier, A. K. Applications of isothermal titration calorimetry in pure and applied research from 2016 to 2020. *J. Mol. Recognit.* **2021**, *34*, No. e2901.
- (74) Lin, K.; Wu, G. Isothermal Titration Calorimetry Assays to Measure Binding Affinities In Vitro. *Methods in Molecular Biology*; Springer, 2019; Vol. 1893, pp 257–272.
- (75) Claveria-Gimeno, R.; Vega, S.; Abian, O.; Velazquez-Campoy, A. A look at ligand binding thermodynamics in drug discovery. *Expert Opin Drug Discovery* **2017**, *12*, 363–377.
- (76) Beigoli, S.; Sharifi Rad, A.; Askari, A.; Assaran Darban, R.; Chamani, J. Isothermal titration calorimetry and stopped flow circular dichroism investigations of the interaction between lomefloxacin and human serum albumin in the presence of amino acids. *J. Biomol. Struct. Dyn.* **2019**, *37*, 2265–2282.
- (77) Marjani, N.; Dareini, M.; Asadzade-Lotfabad, M.; Pejhan, M.; Mokaberi, P.; Amiri-Tehranizadeh, Z.; Saberi, M. R.; Chamani, J. Evaluation of the binding effect and cytotoxicity assay of 2-Ethyl-5-(4-methylphenyl) pyrimido pyrazole ophthalazine trione on calf thymus DNA: spectroscopic, calorimetric, and molecular dynamics approaches. *Luminescence* **2022**, *37*, 310–322.
- (78) Rabbani, G.; Baig, M. H.; Lee, E. J.; Cho, W. K.; Ma, J. Y.; Choi, I. Biophysical Study on the Interaction between Eperisone Hydrochloride and Human Serum Albumin Using Spectroscopic, Calorimetric, and Molecular Docking Analyses. *Mol. Pharmaceutics* **2017**, *14*, 1656–1665.
- (79) Lu, H.; Iuliano, J. N.; Tonge, P. J. Structure–kinetic relationships that control the residence time of drug–target complexes: insights from molecular structure and dynamics. *Curr. Opin. Chem. Biol.* **2018**, *44*, 101–109.
- (80) Tummino, P. J.; Copeland, R. A. Residence time of receptor–ligand complexes and its effect on biological function. *Biochemistry* **2008**, *47*, 5481–5492.
- (81) Swinney, D. C. Biochemical mechanisms of drug action: what does it take for success? *Nat. Rev. Drug Discovery* **2004**, *3*, 801–808.
- (82) Copeland, R. A.; Pompliano, D. L.; Meek, T. D. Drug-target residence time and its implications for lead optimization. *Nat. Rev. Drug Discovery* **2006**, *5*, 730–739.
- (83) Bernetti, M.; Masetti, M.; Rocchia, W.; Cavalli, A. Kinetics of Drug Binding and Residence Time. *Annu. Rev. Phys. Chem.* **2019**, *70*, 143–171.
- (84) Copeland, R. A. The drug-target residence time model: a 10-year retrospective. *Nat. Rev. Drug Discovery* **2016**, *15*, 87–95.
- (85) Dahl, G.; Akerud, T. Pharmacokinetics and the drug-target residence time concept. *Drug Discovery Today* **2013**, *18*, 697–707.
- (86) Lu, H.; Tonge, P. J. Drug-target residence time: critical information for lead optimization. *Curr. Opin. Chem. Biol.* **2010**, *14*, 467–474.
- (87) Copeland, R. A. Evolution of the drug-target residence time model. *Expert Opin Drug Discovery* **2021**, *16*, 1441–1451.
- (88) Bohnert, T.; Gan, L. S. Plasma protein binding: from discovery to development. *J. Pharm. Sci.* **2013**, *102*, 2953–2994.
- (89) Jones, G. A.; Bradshaw, D. S. Resonance Energy Transfer: From Fundamental Theory to Recent Applications. *Front. Phys.* **2019**, *7*, No. 100.
- (90) Wu, P.; Brand, L. Resonance energy transfer: methods and applications. *Anal. Biochem.* **1994**, *218*, 1–13.
- (91) Algar, W. R.; Hildebrandt, N.; Vogel, S. S.; Medintz, I. L. FRET as a biomolecular research tool — understanding its potential while avoiding pitfalls. *Nat. Methods* **2019**, *16*, 815–829.
- (92) Gadella, T. W., Jr.; van der Krogt, G. N.; Bisseling, T. GFP-based FRET microscopy in living plant cells. *Trends Plant Sci.* **1999**, *4*, 287–291.
- (93) Chen, H.; Puhl, H. L., 3rd; Koushik, S. V.; Vogel, S. S.; Ikeda, S. R. Measurement of FRET efficiency and ratio of donor to acceptor concentration in living cells. *Biophys. J.* **2006**, *91*, L39–L41.
- (94) Juárez, J.; Taboada, P.; Mosquera, V. Existence of different structural intermediates on the fibrillation pathway of human serum albumin. *Biophys. J.* **2009**, *96*, 2353–2370.
- (95) Rahman, S.; Rehman, M. T.; Rabbani, G.; Khan, P.; AlAjmi, M. F.; Hassan, M. I.; Muteeb, G.; Kim, J. Insight of the Interaction between 2,4-thiazolidinedione and Human Serum Albumin: A Spectroscopic, Thermodynamic and Molecular Docking Study. *Int. J. Mol. Sci.* **2019**, *20*, No. 2727.
- (96) Tang, B.; Tang, P.; He, J.; Yang, H.; Li, H. Characterization of the binding of a novel antitumor drug ibrutinib with human serum

albumin: Insights from spectroscopic, calorimetric and docking studies. *J. Photochem. Photobiol., B* **2018**, *184*, 18–26.

(97) Wu, D.; Liu, D.; Zhang, Y.; Zhang, Z.; Li, H. Unravelling the binding mechanism of benproperine with human serum albumin: A docking, fluorometric, and thermodynamic approach. *Eur. J. Med. Chem.* **2018**, *146*, 245–250.

(98) Yang, H.; Huang, Y.; Wu, D.; Yan, J.; He, J.; Li, H. In vitro investigation of the interaction between the hepatitis C virus drug sofosbuvir and human serum albumin through ¹H NMR, molecular docking, and spectroscopic analyses. *New J. Chem.* **2016**, *40*, 2530–2540.

(99) Fasano, M.; Curry, S.; Terreno, E.; Galliano, M.; Fanali, G.; Narciso, P.; Notari, S.; Ascenzi, P. The extraordinary ligand binding properties of human serum albumin. *IUBMB Life* **2005**, *57*, 787–796.

(100) Sudlow, G.; Birkett, D. J.; Wade, D. N. The characterization of two specific drug binding sites on human serum albumin. *Mol. Pharmacol.* **1975**, *11*, 824–832.

(101) De Simone, G.; di Masi, A.; Ascenzi, P. Serum Albumin: A Multifaced Enzyme. *Int. J. Mol. Sci.* **2021**, *22*, No. 10086.

(102) Leboffe, L.; di Masi, A.; Polticelli, F.; Trezza, V.; Ascenzi, P. Structural Basis of Drug Recognition by Human Serum Albumin. *Curr. Med. Chem.* **2020**, *27*, 4907–4931.

(103) Zsila, F. Subdomain IB Is the Third Major Drug Binding Region of Human Serum Albumin: Toward the Three-Sites Model. *Mol. Pharmaceutics* **2013**, *10*, 1668–1682.